ARTICLE

Evidence for early life in Earth's oldest hydrothermal vent precipitates

Matthew S. Dodd[1,2], Dominic Papineau[1,2], Tor Grenne[3], John F. Slack[4], Martin Rittner[2], Franco Pirajno[5], Jonathan O'Neil[6] & Crispin T. S. Little[7]

Although it is not known when or where life on Earth began, some of the earliest habitable environments may have been submarine–hydrothermal vents. Here we describe putative fossilized microorganisms that are at least 3,770 million and possibly 4,280 million years old in ferruginous sedimentary rocks, interpreted as seafloor–hydrothermal vent–related precipitates, from the Nuvvuagittuq belt in Quebec, Canada. These structures occur as micrometre–scale haematite tubes and filaments with morphologies and mineral assemblages similar to those of filamentous microorganisms from modern hydrothermal vent precipitates and analogous microfossils in younger rocks. The Nuvvuagittuq rocks contain isotopically light carbon in carbonate and carbonaceous material, which occurs as graphitic inclusions in diagenetic carbonate rosettes, apatite blades intergrown among carbonate rosettes and magnetite–haematite granules, and is associated with carbonate in direct contact with the putative microfossils. Collectively, these observations are consistent with an oxidized biomass and provide evidence for biological activity in submarine–hydrothermal environments more than 3,770 million years ago.

There are no confirmed microfossils older than 3,500 million (Myr) on Earth, probably because of the highly metamorphosed nature of the oldest sedimentary rocks[1]. Therefore, studies have focused almost exclusively on chemical traces and primarily on the isotopic composition of carbonaceous material, which has led to controversies regarding the origin of isotopically light reduced carbon[2]. Schists from the approximately 3,700-Myr-old Isua supracrustal belt in southwest Greenland contain up to 8.8 wt% graphitic carbon that is depleted in ^{13}C, and this depletion has been attributed to biological activity[3,4]. However, because non-biological decarbonation reactions and Fischer-Tropsch-type synthesis[5] can produce reduced carbon with similar isotopic compositions, non-biological interpretations are possible[2]. Apatite with graphite coatings, within iron formations from the approximately 3,830-Myr-old Akilia supracrustal belt in southwest Greenland, has been interpreted as the metamorphosed product of biogenic matter[6], supported by the presence of biologically important heteroatoms within the graphite[7]. However, it has been suggested that some graphite in the Akilia iron formations was deposited by metamorphic fluids[8,9]. This latter interpretation is echoed in the Nuvvuagittuq supracrustal belt (NSB) by the presence of poorly crystalline, fluid-deposited graphite that coats apatite[10], demonstrating that some apatite–graphite occurrences are produced abiotically during fluid remobilization and high-grade metamorphism.

The NSB in northeastern Canada represents a fragment of the Earth's primitive mafic oceanic crust. The NSB is composed predominantly of basaltic metavolcanic rocks (Extended Data Fig. 1), which locally preserve pillow lava structures[11] consistent with a submarine setting, and of chemical sedimentary units including iron formations and minor jasper (quartz-rich rocks with haematite and magnetite) and carbonate-bearing iron formations. The iron formation units occur between sequences of tholeiitic and calc-alkaline metabasalts, suggesting deposition at the same stage of volcanic evolution and seafloor-hydrothermal activity. The minimum age for the belt is constrained by cross-cutting trondhjemitic intrusive rocks that yield U-Pb zircon ages of 3,774–3,751 Myr (refs. 12, 13). Furthermore, ^{146}Sm-^{142}Nd systematics suggest an age of 4,280 Myr for the metabasaltic unit of the NSB[14,15]. The exact age of the NSB is debated (see Supplementary Information); nonetheless, the NSB includes one of the oldest—if not the oldest—iron formations known on Earth. The iron formation has seawater-like chemical signatures[16,17] and heavy Fe isotopic compositions[17,18], consistent with formation by the precipitation of iron derived from hydrothermal fluids associated with volcanism[19]. Bulk-rock rare earth element data for the NSB jasper and carbonate iron formations—especially the presence of positive Eu anomalies—suggest a link to seafloor-hydrothermal activity (Extended Data Fig. 2). The presence of well-preserved, 20–3,000-μm chalcopyrite crystals within the NSB jasper and carbonate iron formations (Extended Data Fig. 3a) demonstrate the lack of post-depositional oxidation.

Most NSB rocks were subjected to upper amphibolite-facies metamorphism around 2,700 Myr ago[14,20]. Here we describe parts of the NSB that were less affected by deformation (Supplementary Table 4) and focus on sites where the metamorphic grade appears not to have exceeded lower amphibolite facies[17]. This setting is evidenced by local outcrops in the southwestern margins of the belt that preserve primary chert, diagenetic calcite rhombohedra with poikilitic textures, and minerals of low metamorphic grade such as euhedral stilpnomelane and minnesotaite in chert that lack pseudomorphic retrograde textures.

Haematite tubes and filaments

Modern hydrothermal Si-Fe vent deposits host communities of microorganisms, some of which are Fe-oxidizing bacteria that form distinctive tubes and filaments[21–26]. Epifluorescence imaging of modern vent samples has shown that cylindrical casts composed of iron oxyhydroxide are formed by bacterial cells and are undeniably biogenic[25]. Hence, morphologically similar tubes and filaments in ancient jaspers may be taken as biosignatures[25,27–30] that can survive elevated temperatures

[1]London Centre for Nanotechnology, 17-19 Gordon Street, London WC1H 0AH, UK. [2]Department of Earth Sciences, University College London, Gower Street, London WC1E 6BT, UK. [3]Geological Survey of Norway, Leiv Eirikssons vei 39, 7040 Trondheim, Norway. [4]U.S. Geological Survey, National Center, MS 954, Reston, Virginia 20192, USA. [5]Centre for Exploration Targeting, The University of Western Australia, 35 Stirling Highway, Crawley, Western Australia 6009, Australia. [6]Department of Earth and Environmental Sciences, University of Ottawa, Ottawa, K1N 6N5, Canada. [7]School of Earth and Environment, University of Leeds, Leeds LS2 9JT, UK.
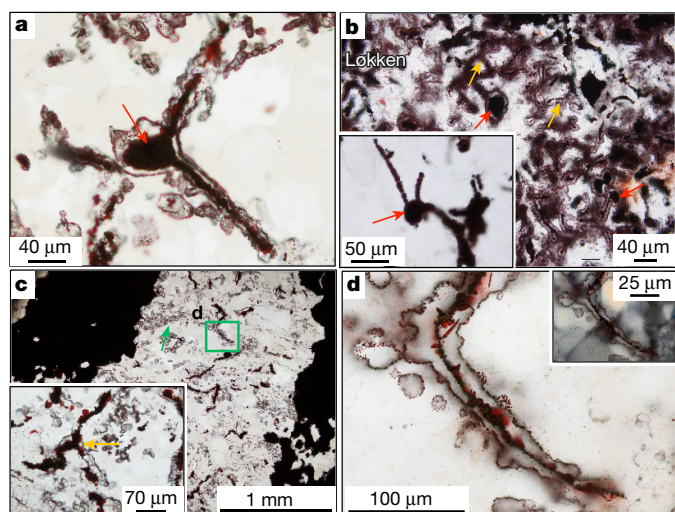
Figure 1 | Transmitted light images of haematite filaments from the NSB and Løkken jaspers. a, Filaments from the NSB attached to a terminal knob (arrow) coated with nanoscopic haematite. **b**, Filaments from the Løkken jaspers coated with nanoscopic haematite and attached to terminal knobs (red arrows) and branching (orange arrows). Inset, multiple filaments attached to a terminal knob. **c**, Filaments from the NSB in quartz band with haematite rosettes (green arrow). Inset, branching filament (orange arrow). Green box defines **d**. **d**, Filament from the NSB enveloped in haematite (inset, same image in cross polars).

and pressures[31], even though such jaspers generally lack carbonaceous material[22,28,32,33]. The presence of abundant microcrystalline quartz in jaspers may provide strong protection of primary features, such that deformation and metamorphism do not obliterate all depositional and diagenetic textures preserved by haematite[29].

Haematite filaments in the NSB jasper are between 2 and 14 μm in diameter and up to 500 μm in length (Fig. 1; Extended Data Fig. 4). Some of the filaments exhibit loose coils (Extended Data Fig. 4a), some are branched (Fig. 1c), and some form twisting plates of haematite around a core that radiate from terminal knobs (Extended Data Fig. 4e, f). They occur within quartz layers of the jaspers, in millimetre-sized domains together with haematite rosettes (Fig. 1c), and comprise micrometre-sized grains of haematite that are in turn enveloped by nanoscale haematite (Fig. 1d). Cross-polar images show that the filaments do not occur along grain boundaries (Fig. 1d). Some filaments are associated with micrometre-sized carbonate grains, which locally occur together with graphite (Extended Data Fig. 5). The NSB filaments (Fig. 1a–d) have morphologies and compositions similar to those of filaments that occur commonly in Phanerozoic jaspers of seafloor-hydrothermal origin, such as those from Løkken, Norway (see Supplementary Information; approximately 480 Myr; Fig. 1b) and the Franciscan Complex, California,

USA (approximately 185 Myr)[33]. The NSB filaments are also similar to microbial filaments found in modern, low-temperature hydrothermal vents[23,26], some of which display twisted and branched morphologies known to be formed by iron-oxidizing bacteria[21,26,30].

Within the NSB jasper, cylindrical tubes with walls composed of dense nanoscale haematite grains are preserved within coarse (50–500 μm) quartz, which encapsulates the entire structure and fills the centres (Fig. 2). Depth reconstructions demonstrate the consistent shape of the tubes and filaments along their lengths and the cylindrical morphology of the tubes in three dimensions (Fig. 2b, Extended Data Fig. 4). The tubes are straight, have diameters of 16–30 μm (Extended Data Fig. 4), and vary in length from 80 to 400 μm. Most tubes are filled with quartz only, but some encapsulate a filament composed of micrometre-sized, platy grains of haematite that extend radially outward from the core of the filament (Fig. 2c), similar to those in younger jaspers (Fig. 2g). The NSB tubes form aligned clusters within patches of locally coarser quartz (Fig. 2a, e), similar to tubes in the Løkken jaspers (Fig. 2h), and occur in lamination-deflecting, concretionary structures (Extended Data Fig. 3b, c) and within quartz layers between millimetre-thick haematite–magnetite layers (Extended Data Fig. 3f). About one in ten tubes in the NSB terminate with a haematite knob (80–120 μm in diameter); about half of those have a second tube attached (Figs 1a, 2f).

The tubes exhibit features attributed in other seafloor-hydrothermal jaspers to fossil remains of iron-oxidizing bacteria[28]: 1, tubes contain internal haematite filaments, similar to those of modern microbial remains[23,26]; 2, some tubes are attached to terminal haematite knobs, like microbial tubes documented throughout the geological record[28,32] and in modern hydrothermal precipitates[21,24]; 3, uniform tube diameters are in the same 16–30-μm range as those of tube microfossils in the Mt. Windsor and Uralian jaspers[29,34]; 4, tubes are aligned in a similar direction (as in some ancient jaspers[34]), which is characteristic of some modern iron-oxidizing bacteria[24,28,30,35]; and 5, tubes and filaments co-occur with apatite, carbonate, and carbonaceous material, as in microfossils within the Løkken (Extended Data Fig. 5) and other Phanerozoic jaspers[36].

To assess the biogenicity of the NSB putative microfossils we consider as a null hypothesis plausible abiogenic mechanisms that could create haematite tubes and filaments through metamorphic stretching or diagenetic processes (see Supplementary Information), such as fluid flow, precipitation reactions, and self-assembly. However, no known mechanism can wholly facilitate the growth of multiple tubes from a single haematite knob at varying angles (Fig. 1a, Extended Data Fig. 4) during metamorphic or diagenetic reactions, together with the formation of internal coiled, branched, and twisted filaments (Extended Data Fig. 4) with haematite envelopes (Fig. 1d), in addition to their close spatial association with carbonate and graphitic carbon (Extended Data Fig. 5). Collectively, our observations cannot be explained by a single or combined abiogenic pathway, and therefore we reject the null hypothesis.
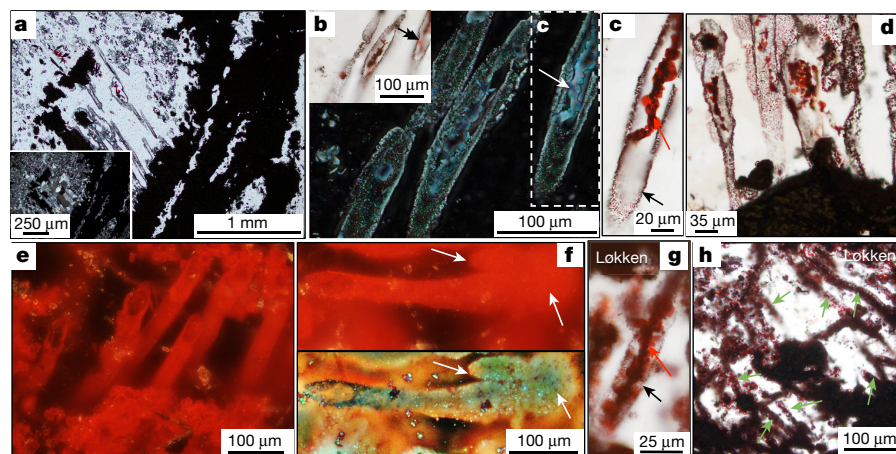

Figure 2 | Transmitted light images of haematite tubes in the NSB and Løkken jaspers. a–f, Tubes from the NSB. **a**, Tubes associated with iron oxide band. **b**, Depth reconstruction of tubes with haematite filament (arrow). Inset, image of tubes at the surface. **c**, Tube showing a twisted filament (red arrow) and walls (black arrow). **d**, Strongly deformed tubes. **e**, Depth reconstruction of tubes. **f**, Two tubes attached to terminal knob (arrows); lower image taken in false colour. **g**, **h**, Tubes from the Løkken jaspers. **g**, Tube showing filament (red arrow) and walls (black arrow). **h**, Aligned tubes (green arrows).
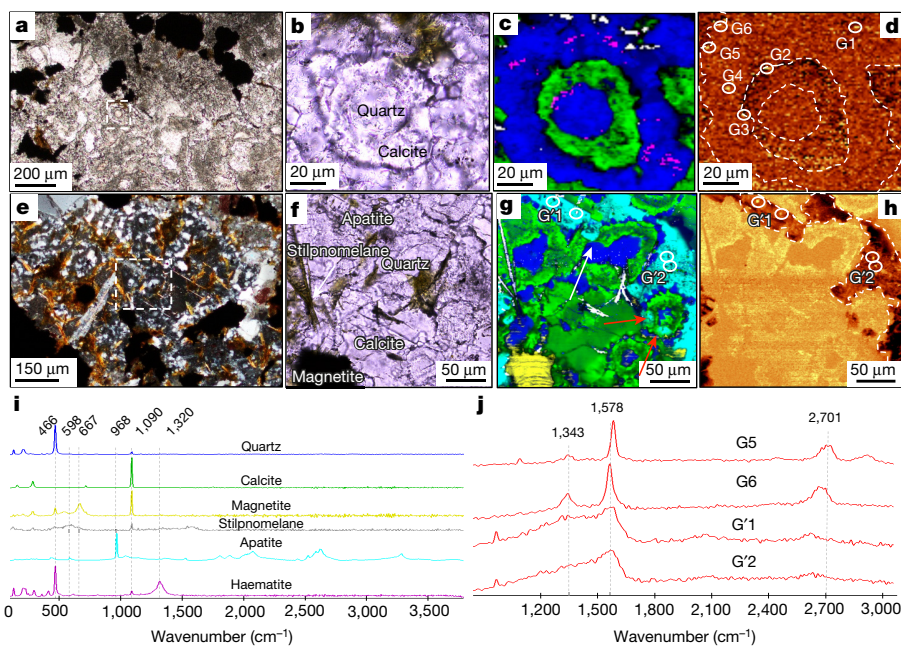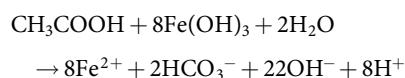
Figure 3 | Carbonate rosettes from the NSB.
a, Transmitted light image of calcite rosettes. Box defines **b**. **b, c**, Transmitted light image in **b** of area targeted by Raman spectroscopy in **c**. **d**, Raman filter map at 1,580 cm^{-1} (width 40 cm^{-1}) with spectra of graphite particles circled. **e**, Transmitted light and cross-polar image of calcite rosettes; box defines **f**. **f, g**, Transmitted light image in **f** of target area shown in **g**. White arrow shows apatite cutting a carbonate rosette; red arrows show apatite inclusions in a carbonate rosette. **h**, Carbonaceous material Raman filter map at 1,565 cm^{-1} (width 50 cm^{-1}). **i, j**, Selected average Raman spectra from maps and carbonaceous material.

Uniformitarianism, epitomised by younger examples of microbially produced haematite tubes in hydrothermal vent precipitates throughout the geological record (Supplementary Table 5), leads us to conclude that haematite tubes and filaments within the NSB jaspers are the mineralized remains of bacterial sheaths and extracellular filaments. Filaments were probably coated by iron oxyhydroxide or silica after being discarded by the microbes, and subsequently coated with silica and recoated by iron oxyhydroxide in successive venting cycles[23,35], producing filament structures that are thicker than the initial structure. Residual carbonaceous material from the microbes is now preserved in association with carbonate in contact with the filaments. Whereas tubes and filaments in younger jaspers are typically attributed to iron oxidizers, other bacteria such as cyanobacteria can produce aligned[37], hollow cylindrical casts of iron oxide[38]. However, the attachment of filaments to terminal knobs is characteristic of some iron oxidizers in hydrothermal systems[21], but not of cyanobacteria. These knobs are morphologically similar to bacterial cells of the anoxygenic photoferrotroph *Hyphomicrobium*, which produces stalks during reproduction. Alternatively, the knobs may be better compared to bacterial holdfasts created by chemolithotroph *Leptothrix*-type bacteria. A twisted morphology in some filaments also closely resembles the iron-rich stalks formed by the extant ζ-proteobacterium *Mariprofundus*.

Carbonate rosettes, apatite and carbonaceous material
If biological processes were involved in the genesis of iron formations, the characteristic absence of carbonaceous material in iron formations could be due to organisms such as photoferrotrophs that separate ferric iron from the cells and allow most carbonaceous material to escape sedimentation[39]. Any carbonaceous material that enters the sediments may be diagenetically oxidized in conjunction with the reduction of ferric iron[40]. This reaction may be understood from the following equation:

$$CH_3COOH + 8Fe(OH)_3 + 2H_2O$$
$$\rightarrow 8Fe^{2+} + 2HCO_3^- + 22OH^- + 8H^+$$

A consequence of this reaction is the oxidation of carbonaceous material to carbonate and the reduction of insoluble ferric iron into soluble ferrous iron, followed by precipitation of iron-bearing carbonate, ferrous silicates, and magnetite. The formation of carbonate from oxidized carbonaceous material is well illustrated in the approximately 2,470-Myr-old Brockman Iron Formation of Western Australia (Extended Data Fig. 6h, i), in which carbonate rhombohedra

occur in layers of disseminated carbonaceous material mixed with carbonate rosettes.

Of particular note is the presence of carbonate rosettes, 50–200 μm in diameter, that typically contain microscopic inclusions of carbonaceous material. Such rosettes are found in the NSB iron formations (Fig. 3, Extended Data Fig. 6) as well as in younger jaspers and iron formations (Supplementary Table 6). In the Løkken jasper, for example, carbonate rosettes with inclusions of carbonaceous material overgrow haematite filaments (Extended Data Fig. 6k) attributed to mineralized bacteria[27]. In this interpretation, carbonaceous material was sourced from the bacteria. Carbonate rosettes have also been grown in diagenetic experiments using ferrihydrite and carbonaceous material[40].

Both NSB and ancient jaspers, and modern hydrothermal vent precipitates, commonly preserve haematite rosettes[27,32,41] (Supplementary Table 7, Extended Data Fig. 7), albeit of debated origin[42]. Ferrihydrite rosettes that form today in the Lau Basin are intimately associated with microbial filaments, but may be a result of abiogenic precipitation[41]. In the Løkken jaspers, haematite rosettes are attributed to Fe-Si gel maturation on the seafloor[27]. Such textural relationships may require micro-chemical Eh–pH gradients that reduce ferric iron, followed by mobilization and oxidation of Fe^{2+} and its re-precipitation as haematite. Given the close proximity of haematite rosettes to microbial filaments in modern vent precipitates[41], it is plausible that microbial carbonaceous material served as a reductant and ferrihydrite as an oxidant.

Sub-spheroidal rosettes of iron calcite (Supplementary Table 8) in carbonate-rich iron formations from the NSB (Fig. 3, Extended Data Fig. 6a, b) have quartz cores and dimensions of approximately 50–200 μm[19]. Some carbonate rosettes locally contain apatite inclusions and are cut by apatite laths hundreds of micrometres in length (Fig. 3g), and by acicular stilpnomelane that cuts both rosettes and apatite (Fig. 3, Extended Data Fig. 6g), demonstrating that the apatite and rosettes are pre-metamorphic. The apatite contains myriad inclusions of aqueous fluid, haematite, magnetite, and carbonaceous material (Fig. 3f–h). Moreover, the rosettes occur with micrometre-sized particles of graphitic carbon, randomly disseminated throughout the rings and surrounding chert (Fig. 3c). Raman spectra of the graphitic carbon show sharp and prominent G-bands ranging from 1,565 to 1,584 cm^{-1} and minor D-bands from 1,331 to 1,349 cm^{-1} (Fig. 3j, Extended Data Fig. 6e). Whereas apatite-hosted carbonaceous material displays Raman G-peak positions consistent with those of graphitic carbon, the broad D-band suggests the presence of disordered sp3-bonded carbon (Fig. 3j) or a contribution from nanoscale haematite, which has
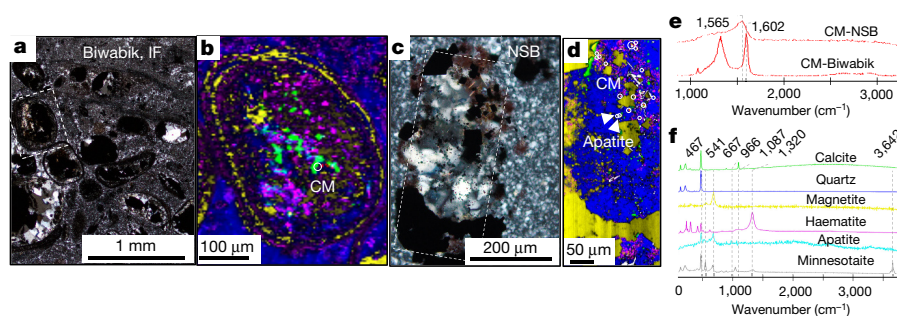
Figure 4 | Granules from the Biwabik and NSB jaspers. a, Cross-polar image of granules in Biwabik jasper. IF, iron formation. **b**, Raman map of area shown with dotted outline in **a**. CM, carbonaceous material. **c**, Cross-polar image of granule in the NSB. **d**, Raman map of area shown with dotted outline in **c**. **e**, **f**, Selected average Raman spectra of carbonaceous material and minerals from maps.

a broad peak at 1,320 cm^{-1}, partly explaining the broad and intense Raman D-peak. Iron oxides can be seen associated with carbonaceous material in transmitted light and by micro-Raman spectroscopy (Extended Data Fig. 8a). Raman spectra of graphitic carbon within the carbonate rosettes (Fig. 3j) yield a range of calculated crystallization temperatures[43] between 396 °C and 564 °C (Supplementary Tables 9, 10), which is partly consistent with mineral geothermometers obtained from the Ujaraaluk amphibolite[17], distinct from those of poorly crystalline, fluid-deposited graphite in silicate iron formations from other parts of the NSB[10] (Extended Data Fig. 8, Supplementary Table 11). Additionally, Raman spectra of graphitic carbon found in layered jaspers of the NSB (Extended Data Fig. 8b–e) show that graphite from two different samples shares common crystallization temperatures of approximately 500 °C. The formation of syngenetic carbon preserved as graphite can be explained by the production of carbonaceous material via abiogenic synthesis[5], carbonate decarbonation[2], or from an original microbial biomass.

Isotopically light carbonate (−15 to −5‰) in iron formations has been attributed to the oxidation of isotopically light carbonaceous material derived from microbial activity[44], but precludes neither the oxidation of isotopically light abiogenic carbonaceous material nor a contribution from marine carbonate. The $\delta^{13}C_{carb}$ and $\delta^{13}C_{org}$ values for jaspers from the NSB are −8.3 to −6.7‰ and −25.7 to −19.7‰, respectively[10], consistent with a biogenic origin, although not unambiguously. However, in the case of the NSB, the phosphorus (an element vital in biology) in laths of apatite intergrown with the graphite-bearing carbonate rosettes suggests a biological source for the carbon in graphite. In modern ocean sediments, accumulations of carbonaceous material on the seafloor may concentrate phosphorus through biological metabolisms[45]. Furthermore, the presence of apatite in some NSB carbonate rosettes is analogous to occurrences of apatite rosettes between stromatolitic phosphorite columns in a flourishing late Palaeoproterozoic microbial ecosystem[46]. Whereas structures similar to carbonate rosettes may form in open spaces and cavities[47], the well-banded, siliceous carbonate gels that formed precursors to these carbonate iron formations could not have had a porous texture, and so the formation of carbonate rosettes by open-space filling can be ruled out. This conclusion is reinforced by the presence of morphologically similar, diagenetic graphite-bearing carbonate rosettes in the Løkken jasper[27] (Extended Data Fig. 6j–m). Combined with evidence of filamentous microfossils and their direct association with carbonate and graphitic carbon, and with numerous other observations supporting biological activity in the NSB, the carbonate rosettes are best explained as having formed by the oxidation of biomass. Such reactions may have proceeded as chemically oscillating reactions akin to the Belousov–Zhabotinsky reaction[48], in line with inferences from similar structures in younger iron formations (Extended Data Fig. 6h–m) and diagenetic experiments[40].

Granules

Magnetite-rimmed granules are common in late Palaeoproterozoic iron formations and typically occur between stromatolite columns (Extended Data Fig. 3i) and host microfossils. The oldest known granular iron formation from the Mozaan Group in South Africa is about 2,900 Myr old and contains magnetite-rimmed granules, isotopically light carbonate, and zero-to-positive $\delta^{56}Fe$ values, suggesting involvement of iron-oxidizing microbes[49].

Comparable 100–500-μm spheroidal to sub-spheroidal granules occur in the NSB jaspers that crop out together with the carbonate iron formations and banded jaspers hosting the microfossils (Extended Data Fig. 3b, f). These granules occur in a matrix of chert (Fig. 4C) and have rims composed of coarse magnetite with interiors of coarser-grained quartz compared to the matrix. Micro-Raman images reveal that the granules contain micrometre-sized minnesotaite, magnetite, calcite, haematite, apatite, and carbonaceous material (Fig. 4d). The inclusions of carbonaceous material within the granules are 1–4 μm in size and display a predominant Raman peak at about 1,560–1,580 cm^{-1} and a broad, poorly resolved D-peak (Fig. 4e). Granules of a similar size (200–400 μm) in jaspers from the late Palaeoproterozoic Biwabik Iron Formation (Fig. 4a) and the Løkken jasper (Extended Data Fig. 9i) also contain quartz coarser than in the surrounding matrix, and a comparable mineralogy dominated by magnetite-rimmed granules accompanied by haematite, carbonate, carbonaceous material, and ferrous silicates. Carbonaceous material within granules from all of these jaspers is typically associated with, and coats, micrometre-sized diagenetic carbonate (Extended Data Fig. 9). This close spatial association and the occurrence of carbonaceous material concentrated in diagenetic granules suggest that such carbonaceous material is a primary phase. Less commonly, Løkken granules contain haematite filaments with terminal knobs (Extended Data Fig. 9l).

We propose that the mineralogical constituents of iron-oxide granules of these jaspers reflect oxidation–reduction reactions. This model implicates carbonaceous material and ferric iron as original reactants, whereas ferric–ferrous silicates, apatite, magnetite, and carbonate are considered reaction products. Given the similar morphology, mineralogy, and composition, and the common occurrence of rosettes, granules, and filamentous microfossils in the Biwabik, Løkken, and NSB jaspers, these diagenetic reactions would have proceeded in a similar manner. This conclusion and the well-documented occurrence of microfossils within some granules[50] (Extended Data Fig. 9l) point to an origin involving microorganisms on the Nuvvuagittuq seafloor.

Preservation in the NSB of carbonaceous material and minerals in diagenetic rosettes and granules that formed from the oxidation of biomass, together with the presence of tubes similar in mineralogy and morphology to those in younger jaspers interpreted as microfossils, reveal that life established a habitat near submarine-hydrothermal vents before 3,770 Myr ago and possibly as early as 4,280 Myr ago. On the basis of chemical and morphological lines of evidence, the tubes and filaments are best explained as remains of iron-metabolizing filamentous bacteria, and therefore represent the oldest life forms recognized on Earth. Given this new evidence from the NSB, ancient submarine-hydrothermal vent systems should be viewed as potential sites for the origins of life on Earth, and thus primary targets in the search for extraterrestrial life.

1. Bernard, S. & Papineau, D. Graphitic carbons and biosignatures. *Elements* **10,** 435–440 (2014).
2. van Zuilen, M. A., Lepland, A. & Arrhenius, G. Reassessing the evidence for the earliest traces of life. *Nature* **418,** 627–630 (2002).
3. Ohtomo, Y., Kakegawa, T., Ishida, A., Nagase, T. & Rosing, M. T. Evidence for biogenic graphite in early Archaean Isua metasedimentary rocks. *Nat. Geosci.* **7,** 25–28 (2013).
4. Rosing, M. T. ^{13}C-depleted carbon microparticles in >3700-Ma sea-floor sedimentary rocks from West Greenland. *Science* **283,** 674–676 (1999).
5. McCollom, T. M. & Seewald, J. S. Abiotic synthesis of organic compounds in deep-sea hydrothermal environments. *Chem. Rev.* **107,** 382–401 (2007).
6. Mojzsis, S. J. et al. Evidence for life on Earth before 3,800 million years ago. *Nature* **384,** 55–59 (1996).
7. Papineau, D. et al. Ancient graphite in the Eoarchean quartz-pyroxene rocks from Akilia in southern West Greenland II: isotopic and chemical compositions and comparison with Paleoproterozoic banded iron formations. *Geochim. Cosmochim. Acta* **74,** 5884–5905 (2010).
8. Papineau, D. et al. Ancient graphite in the Eoarchean quartz–pyroxene rocks from Akilia in southern West Greenland I: petrographic and spectroscopic characterization. *Geochim. Cosmochim. Acta* **74,** 5862–5883 (2010).
9. Lepland, A., van Zuilen, M. A. & Philippot, P. Fluid-deposited graphite and its geobiological implications in Early Archean gneiss from Akilia, Greenland. *Geobiology* **9,** 2–9 (2011).
10. Papineau, D. et al. Young poorly crystalline graphite in the >3.8-Gyr-old Nuvvuagittuq banded iron formation. *Nat. Geosci.* **4,** 376–379 (2011).
11. O'Neil, J., Francis, D. & Carlson, R. W. Implications of the Nuvvuagittuq greenstone belt for the formation of Earth's early crust. *J. Petrol.* **52,** 985–1009 (2011).
12. Cates, N. L., Ziegler, K., Schmitt, A. K. & Mojzsis, S. J. Reduced, reused and recycled: detrital zircons define a maximum age for the Eoarchean (ca. 3750–3780 Ma) Nuvvuagittuq supracrustal belt, Québec (Canada). *Earth Planet. Sci. Lett.* **362,** 283–293 (2013).
13. Darling, J. R. et al. Eoarchean to Neoarchean evolution of the Nuvvuagittuq supracrustal belt: new insights from U-Pb zircon geochronology. *Am. J. Sci.* **313,** 844–876 (2013).
14. O'Neil, J., Carlson, R. W., Paquette, J.-L. & Francis, D. Formation age and metamorphic history of the Nuvvuagittuq greenstone belt. *Precambr. Res.* **220–221,** 23–44 (2012).
15. O'Neil, J., Carlson, R. W., Francis, D. & Stevenson, R. K. Neodymium-142 evidence for Hadean mafic crust. *Science* **321,** 1828–1831 (2008).
16. Mloszewska, A. M. et al. The composition of Earth's oldest iron formations: the Nuvvuagittuq supracrustal belt (Québec, Canada). *Earth Planet. Sci. Lett.* **317–318,** 331–342 (2012).
17. O'Neil, J. et al. in *Earth's Oldest Rocks* Vol. 15 (eds van Kranendonk, M. J., Smithies, R. H. & Bennett, V. C.) 219–250 (Elsevier, 2007).
18. Dauphas, N., Cates, N. L., Mojzsis, S. J. & Busigny, V. Identification of chemical sedimentary protoliths using iron isotopes in the >3750 Ma Nuvvuagittuq supracrustal belt, Canada. *Earth Planet. Sci. Lett.* **254,** 358–376 (2007).
19. Mloszewska, A. M. et al. Chemical sedimentary protoliths in the >3.75Ga Nuvvuagittuq supracrustal belt (Québec, Canada). *Gondwana Res.* **23,** 574–594 (2013).
20. Cates, N. L. & Mojzsis, S. J. Metamorphic zircon, trace elements and Neoarchean metamorphism in the ca. 3.75 Ga Nuvvuagittuq supracrustal belt, Québec (Canada). *Chem. Geol.* **261,** 99–114 (2009).
21. Edwards, K. J. et al. Ultra-diffuse hydrothermal venting supports Fe-oxidizing bacteria and massive umber deposition at 5000 m off Hawaii. *ISME J.* **5,** 1748–1758 (2011).
22. Juniper, S. K. & Fouquet, Y. Filamentous iron-silica deposits from modern and ancient hydrothermal sites. *Can. Mineral.* **26,** 859–869 (1988).
23. Li, J. et al. Microbial diversity and biomineralization in low-temperature hydrothermal iron-silica-rich precipitates of the Lau Basin hydrothermal field. *FEMS Microbiol. Ecol.* **81,** 205–216 (2012).
24. Boyd, T. D. & Scott, S. D. Microbial and hydrothermal aspects of ferric oxyhydroxides and ferrosic hydroxides: the example of Franklin Seamount, western Woodlark Basin, Papua New Guinea. *Geochem. Trans.* **2,** 45 (2001).
25. Emerson, D. & Moyer, C. L. Neutrophilic Fe-oxidizing bacteria are abundant at the Loihi Seamount hydrothermal vents and play a major role in Fe oxide deposition. *Appl. Environ. Microbiol.* **68,** 3085–3093 (2002).
26. Hein, J. R., Clague, D. A., Koski, R. A., Embley, R. W. & Dunham, R. E. Metalliferous sediment and a silica-hematite deposit within the Blanco Fracture Zone, northeast Pacific. *Mar. Georesour. Geotechnol.* **26,** 317–339 (2008).
27. Grenne, T. & Slack, J. F. Bedded jaspers of the Ordovician Løkken ophiolite, Norway: seafloor deposition and diagenetic maturation of hydrothermal plume-derived silica-iron gels. *Miner. Depos.* **38,** 625–639 (2003).
28. Little, C. T. S., Glynn, S. E. J. & Mills, R. A. Four-hundred-and-ninety-million-year record of bacteriogenic iron oxide precipitation at sea-floor hydrothermal vents. *Geomicrobiol. J.* **21,** 415–429 (2004).
29. Duhig, N. C., Stolz, J., Davidson, G. J. & Large, R. R. Cambrian microbial and silica gel textures in silica iron exhalites from the Mount Windsor volcanic belt, Australia: their petrography, chemistry, and origin. *Econ. Geol.* **87,** 764–784 (1992).
30. Krepski, S. T., Emerson, D., Hredzak-Showalter, P. L., Luther, G. W., III & Chan, C. S. Morphology of biogenic iron oxides records microbial physiology and environmental conditions: toward interpreting iron microfossils. *Geobiology* **11,** 457–471 (2013).
31. Picard, A., Obst, M., Schmid, G., Zeitvogel, F. & Kappler, A. Limited influence of Si on the preservation of Fe mineral-encrusted microbial cells during experimental diagenesis. *Geobiology* **14,** 276–292 (2016).
32. Chi Fru, E. et al. Biogenicity of an early Quaternary iron formation, Milos Island, Greece. *Geobiology* **13,** 225–244 (2015).
33. Little, C. T. S., Herrington, R., Haymon, R. & Danelian, T. Early Jurassic hydrothermal vent community from the Franciscan Complex, San Rafael Mountains. *Calif. Geol.* **27,** 167–170 (1999).
34. Ayupova, N. R. & Maslennikov, V. V. Biomorphic textures in the ferruginous-siliceous rocks of massive sulfide-bearing paleohydrothermal fields in the Urals. *Lithol. Miner. Resour.* **48,** 438–455 (2013).
35. Sun, Z. et al. Generation of hydrothermal Fe-Si oxyhydroxide deposit on the southwest Indian Ridge and its implication for the origin of ancient banded iron formations. *J. Geophys. Res. Biogeosci.* **120,** 187–203 (2015).
36. Ayupova, N. R., Maslennikov, V. V., Sadykov, S. A., Maslennikova, S. P. & Danyushevsky, L. V. in *Biogenic–Abiogenic Interactions in Natural and Anthropogenic Systems* (eds Frank-Kamenetskaya, V. O., Panova, G. E. & Vlasov, Y. D.) 109–122 (Springer, 2016).
37. Campbell, K. A. et al. Tracing biosignature preservation of geothermally silicified microbial textures into the geological record. *Astrobiology* **15,** 858–882 (2015).
38. Parenteau, M. N. & Cady, S. L. Microbial biosignatures in iron-mineralized phototrophic mats at Chocolate Pots Hot Springs, Yellowstone National Park, United States. *Palaios* **25,** 97–111 (2010).
39. Thompson, K. J., Lliros, M., Michiels, C., Kenward, P. & Crowe, S. in *2014 GSA Annual Meeting* Vol. 46, 401 (Geol. Soc. Am. Abstracts with Programs, 2014).
40. Köhler, I., Konhauser, K. O., Papineau, D., Bekker, A. & Kappler, A. Biological carbon precursor to diagenetic siderite with spherical structures in iron formations. *Nat. Commun.* **4,** 1741 (2013).
41. Sun, Z. et al. Mineralogical characterization and formation of Fe-Si oxyhydroxide deposits from modern seafloor hydrothermal vents. *Am. Mineral.* **98,** 85–97 (2012).
42. Heaney, P. J. & Veblen, D. R. An examination of spherulitic dubiomicrofossils in Precambrian banded iron formations using the transmission electron microscope. *Precambr. Res.* **49,** 355–372 (1991).
43. Beyssac, O., Goffe, B., Chopin, C. & Rouzaud, J. N. Raman spectra of carbonaceous material in metasediments: a new geothermometer. *J. Metamorph. Geol.* **20,** 859–871 (2002).
44. Heimann, A. et al. Fe, C, and O isotope compositions of banded iron formation carbonates demonstrate a major role for dissimilatory iron reduction in ~2.5 Ga marine environments. *Earth Planet. Sci. Lett.* **294,** 8–18 (2010).
45. Cappellen, P. V. & Berner, R. A. A mathematical model for the early diagenesis of phosphorus and fluorine in marine sediments: apatite precipitation. *Am. J. Sci.* **288,** 289–333 (1988).
46. Papineau, D. et al. Nanoscale petrographic and geochemical insights on the origin of the Palaeoproterozoic stromatolitic phosphorites from Aravalli Supergroup, India. *Geobiology* **14,** 3–32 (2016).
47. Brasier, A. T., Rogerson, M. R., Mercedes-Martin, R., Vonhof, H. B. & Reijmer, J. J. G. A test of the biogenicity criteria established for microfossils and stromatolites on Quaternary tufa and speleothem materials formed in the "Twilight Zone" at Caerwys, UK. *Astrobiology* **15,** 883–900 (2015).
48. Zaikin, A. N. & Zhabotinsky, A. M. Concentration wave propagation in two-dimensional liquid-phase self-oscillating system. *Nature* **225,** 535–537 (1970).
49. Smith, A. J. B., Beukes, N. J., Gutzmer, J., Johnson, C. M. & Czaja, A. D. in *Goldschmidt.* 2384 (Mineralogical Society, 2012).
50. Walter, M. R., Goode, A. D. T. & Hall, W. D. M. Microfossils from a newly discovered Precambrian stromatolitic iron formation in Western Australia. *Nature* **261,** 221–223 (1976).

Supplementary Information is available in the online version of the paper.

METHODS

Optical microscopy. Standard 30-μm-thick, polished and doubly-polished thin sections and 3-mm-thick polished slabs were prepared with a final polishing step using Al_2O_3 0.5 μm powder for investigation using transmitted and reflected light microscopy. An Olympus BX51 microscope, with 5×, 10×, 20×, 50× and 100× objectives not using immersion oil and CCD camera was used to map petrographic features in thin sections. Depth reconstruction images were formed from multiple images taken at 2-μm intervals through thin sections and recombined utilizing the Z-project function in ImageJ.

Confocal Raman spectroscopy. Micro-Raman microscopy was conducted on petrographic targets within the polished thin sections using a WiTec alpha300 confocal Raman imaging microscope with a 532-nm wavelength laser and operating at a power between 0.1 and 6 mW, depending on the target. Raman spectra and hyperspectral scans were obtained at variable magnifications of 20× to 100× and hence at variable spatial resolutions of up to 360 nm; spectral resolutions of 4 cm^{-1} were achieved using a 600 lines per millimetre grating. Hyperspectral images were created for specific mineral phases using peak intensity mapping for characteristic peaks of each individual mineral in a scan. Average spectra were calculated by creating a mask on homogeneous pixels of individual phases and had their backgrounds fitted to a polynomial function and subtracted. Large area scans (>100 μm × 100 μm) were completed using the same process outlined previously, with spatial resolutions below 10 μm. Peak parameters were calculated from a Lorenz function modelled for each selected peak. Cosmic ray reduction was applied to all Raman spectra.

Scanning electron microscopy. Scanning electron microscopy (SEM) in back-scattered electron and secondary electron imaging modes was used to characterize the morphology and composition of selected targets, which were also characterized by energy-dispersive x-ray spectroscopy (EDS). Analyses were carried out in the Department of Earth Sciences at University College London using a JEOL JSM-6480L SEM. Standard operating conditions for SEM imaging and EDS analysis were 15 kV accelerating voltage, working distance of 10 mm, and electron beam current of 1 nA. Samples were coated with a few nanometres of Au prior to analysis.

Electron probe micro-analysis (EPMA). Major element mineral analyses of minerals were obtained using a JEOL8100 Superprobe (WDS) at Birkbeck College. Analysis was carried out using an accelerating voltage of 15 kV, current of 1 nA, and beam spot diameter of 1 μm. The analyses were calibrated against standards of natural silicates, oxides, and Specpure metals with the data corrected using a ZAF program.

Focused ion beam nano-fabrication. Focused ion beam (FIB) trench milling was performed using a Zeiss 1540 XB FIB-SEM. Targets located by secondary electrons were protected by a 1-μm-thick W shield deposited on the thin section surface. FIB foils were prepared using a focused beam of Ga ions starting with currents of 5 nA and going down to 200 and 100 pA 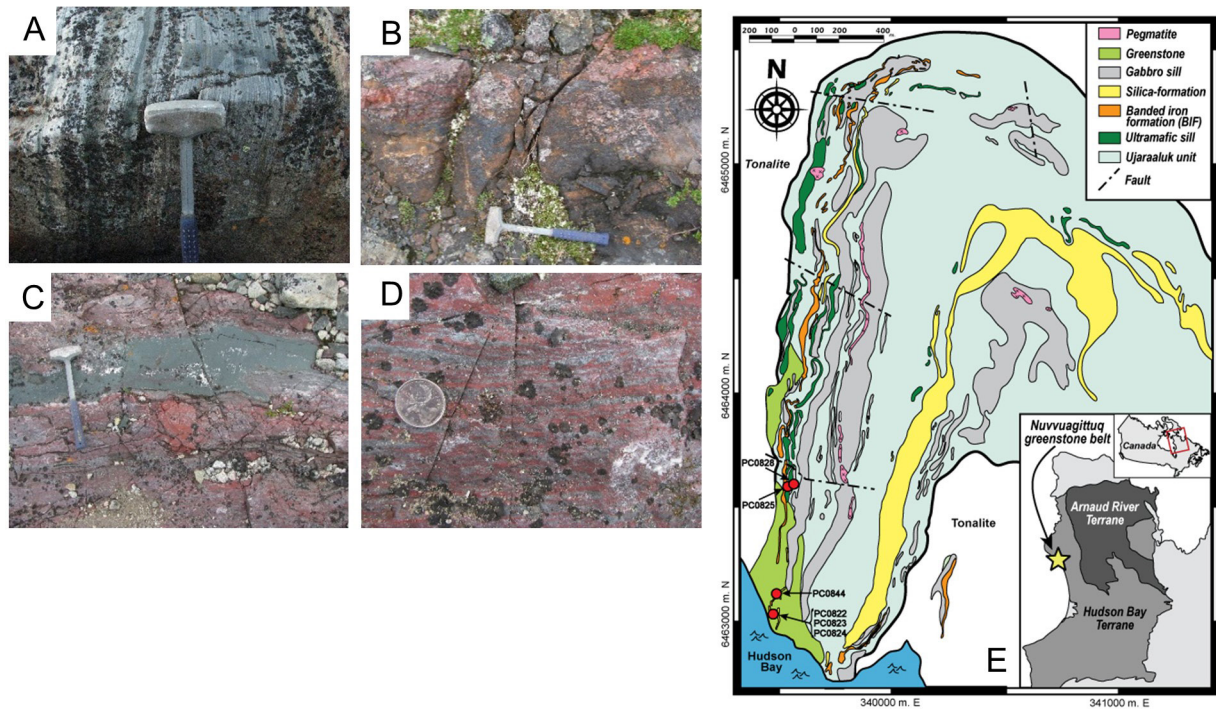for the final steps to expose subsurface minerals, before secondary electron images were acquired. A detailed description of the FIB nano-fabrication procedures can be found elsewhere[52,53].

Inductively coupled plasma-mass spectrometry (ICP-MS). Rare earth element analyses were performed by Activation Laboratories Ltd using a Varian Vista 735 ICP-MS. Yttrium was measured to a detection limit of 2 ppm and all other rare earth elements have detection limits of 0.1 ppm or better.
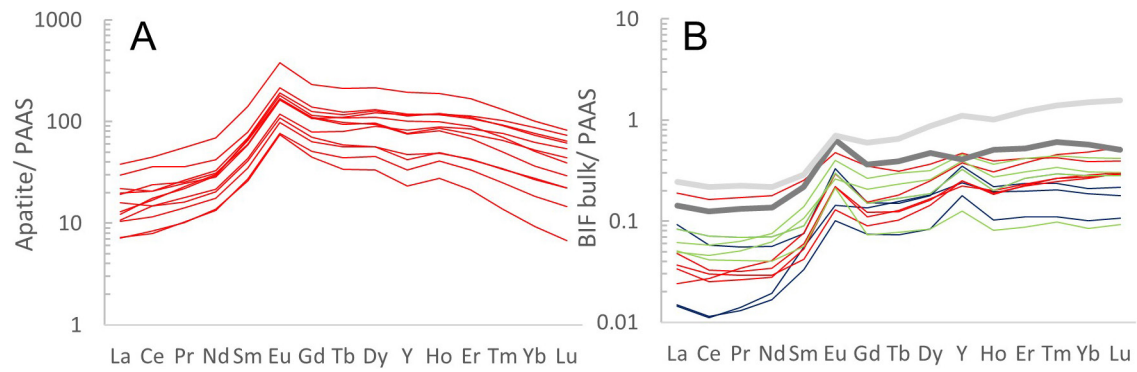
Laser ablation (LA)-ICP-MS. Analyses were conducted at the London Geochronology Centre (LGC), in the Department of Earth Sciences, UCL, utilising an ESI NWR193 laser-ablation system coupled to an Agilent 7700x ICPMS. Instrument parameters are given in Supplementary Tables 1 and 2. LA-ICP-MS procedures were as described[54], with Madagascar Apatite[55] (ID-TIMS age 473.5 ± 0.7 Ma) used as an external age standard for corrections of mass bias and fractionation. Isotopes measured and dwell times are listed in Supplementary Tables 3 and 4. Glitter 4.4[56] was used for data reduction; ages were calculated as described[57], where the calculated $^{206}Pb/^{238}U$ age was used for grains younger than 1,100 Ma, and the $^{207}Pb/^{206}Pb$ age for older grains, rejecting analyses exhibiting more than +5 or −15% discordance. Trace element concentrations were calculated using NIST SRM 612 and 610 glass[58,59] as external standards; ^{44}Ca was used as an internal standard, assuming stoichiometric concentration for apatite.

Data availability statement. The data that support the findings of this study are available from the corresponding author upon reasonable request.
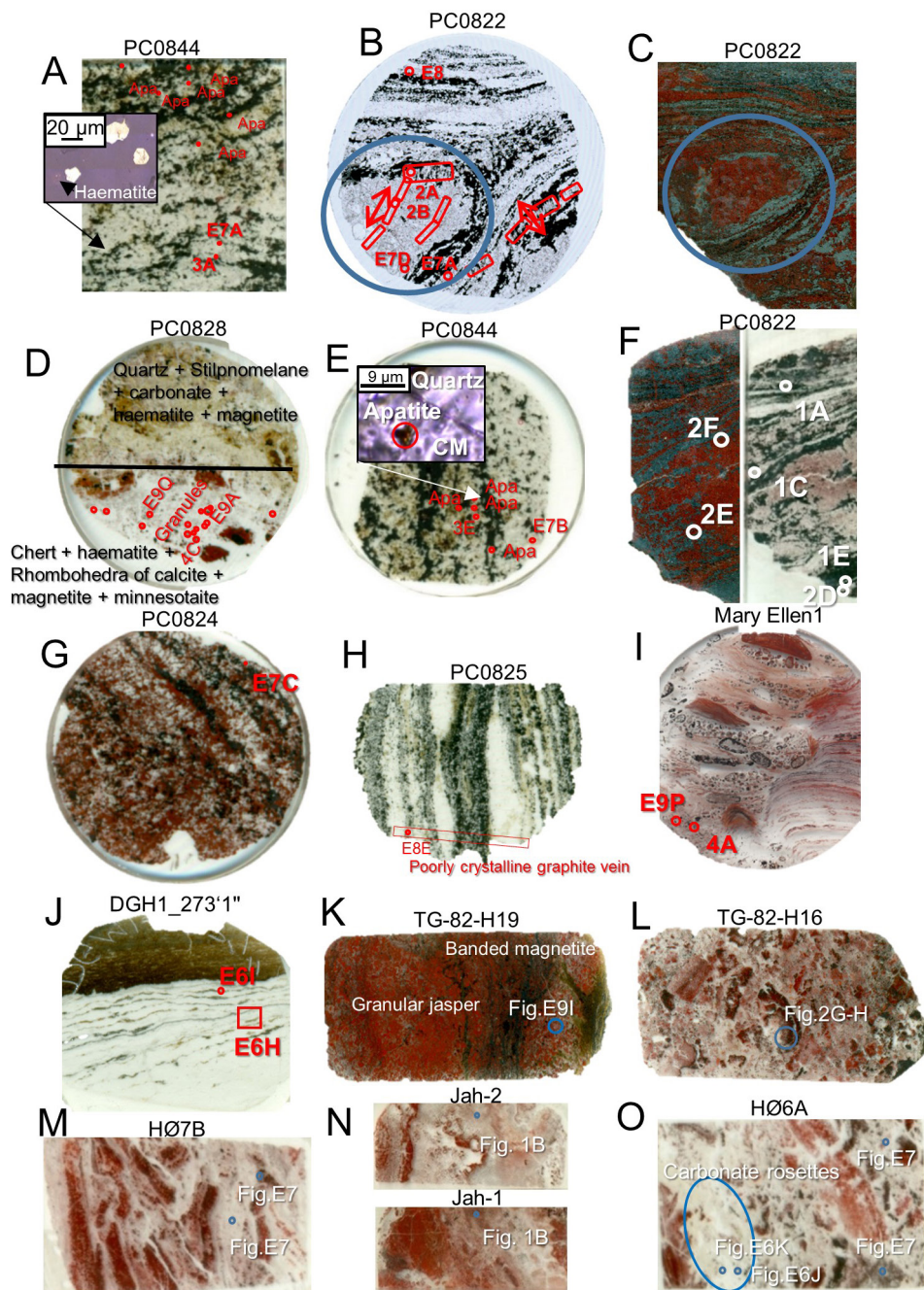
51. Bolhar, R., Kamber, B. S., Moorbath, S., Fedo, C. M. & Whitehouse, M. J. Characterisation of early Archaean chemical sediments by trace element signatures. *Earth Planet. Sci. Lett.* **222,** 43–60 (2004).
52. Wirth, R. Focused Ion Beam (FIB) combined with SEM and TEM: advanced analytical tools for studies of chemical composition, microstructure and crystal structure in geomaterials on a nanometre scale. *Chem. Geol.* **261,** 217–229 (2009).
53. Zega, T. J., Nittler, L. R., Busemann, H., Hoppe, P. & Stroud, R. M. Coordinated isotopic and mineralogic analyses of planetary materials enabled by in situ lift-out with a focused ion beam scanning electron microscope. *Meteorit. Planet. Sci.* **42,** 1–14 (2007).
54. Jackson, S. E., Pearson, N. J., Griffin, W. L. & Belousova, E. A. The application of laser ablation-inductively coupled plasma-mass spectrometry to in situ U–Pb zircon geochronology. *Chem. Geol.* **211,** 47–69 (2004).
55. Chew, D. M., Sylvester, P. J. & Tubrett, M. N. U-Pb and Th-Pb dating of apatite by LA-ICPMS. *Chem. Geol.* **280,** 200–216 (2011).
56. Griffin, W. L., Powell, W. J., Pearson, N. J. & O'Reilly, S. Y. in *Laser Ablation-ICP-MS in the Earth Sciences: Current Practices and Outstanding Issues* Vol. 40 (ed. Sylvester, P. J.) 308–311 (Mineralogical Association of Canada, 2008).
57. Ludwig, K. R. User's Manual for Isoplot 3.70. *Berkeley Geochronology Center Special Publication* **76** (2008).
58. Reed, W. P. Certificate of Analysis, Standard Reference Materials 612 and 613. *Tech. Rep., U. S. National Institute of Standards & Technology* (1992).
59. Jochum, K. P. et al. Determination of reference values for NIST SRM 610-617 glasses following ISO guidelines. *Geostand. Geoanal. Res.* **35,** 397–429 (2011).

Extended Data Figure 1 | Field photographs of the NSB iron formation outcrops. a, Bands of magnetite and chert. **b**, Jasper (top red layer) in contact with Fe-rich carbonate (bottom grey layer). **c**, Layered jaspers with meta-volcanic layers. **d**, Layered jasper; predominantly bands of grey haematite and haematitic chert. **e**, Field location, local geology and sample locations (red spots).
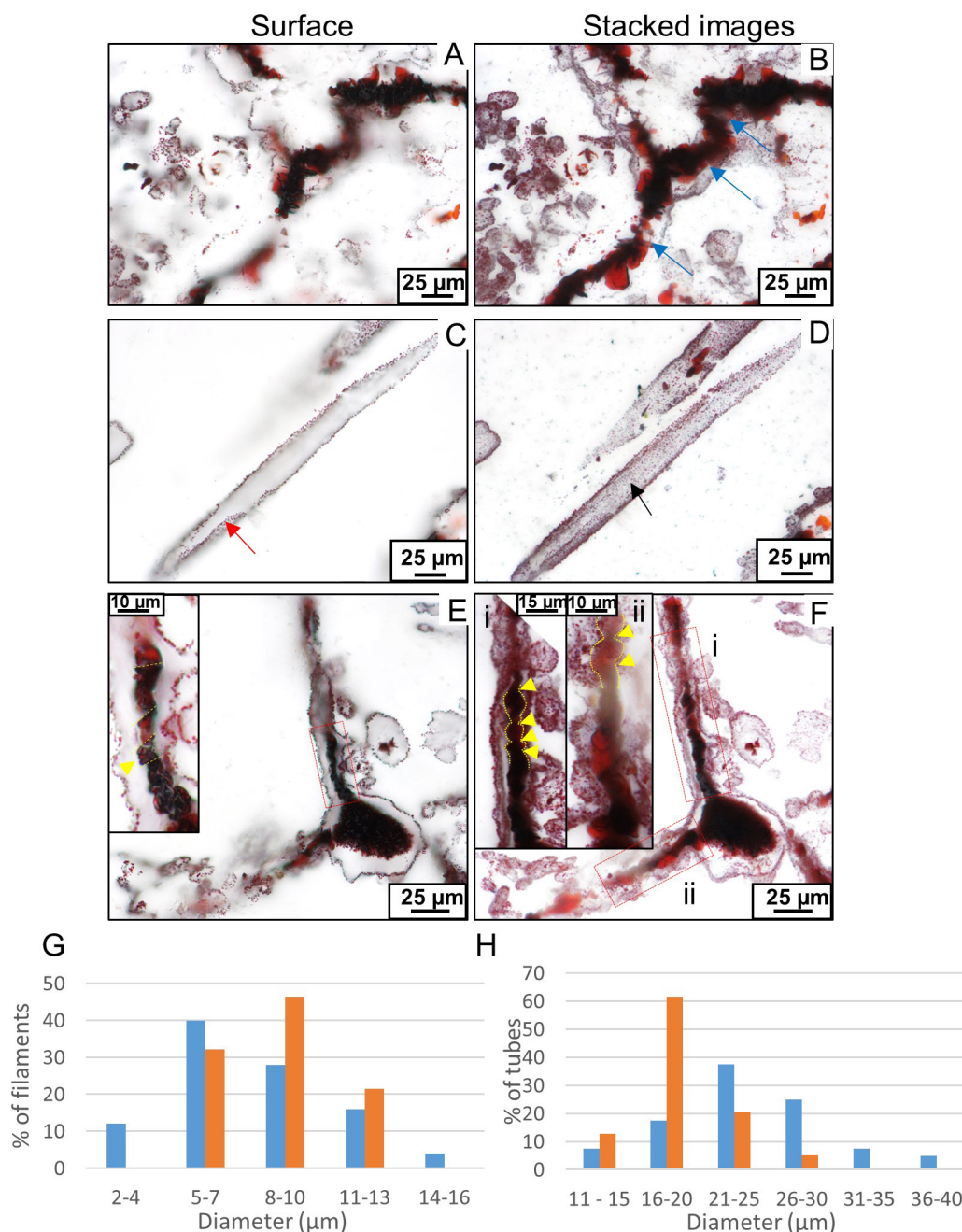
Extended Data Figure 2 | Rare earth element (REE) post-Archean Australian shale (PAAS) normalized plots. a, LA-ICP-MS REE measurements in apatite from PC0844. **b**, Jasper bulk rock REE measurements from PC0824 (dark grey) and PC0844 (light grey). NSB (red[15] and green[16]) and Isua[51] (blue) iron formation bulk rock REE.
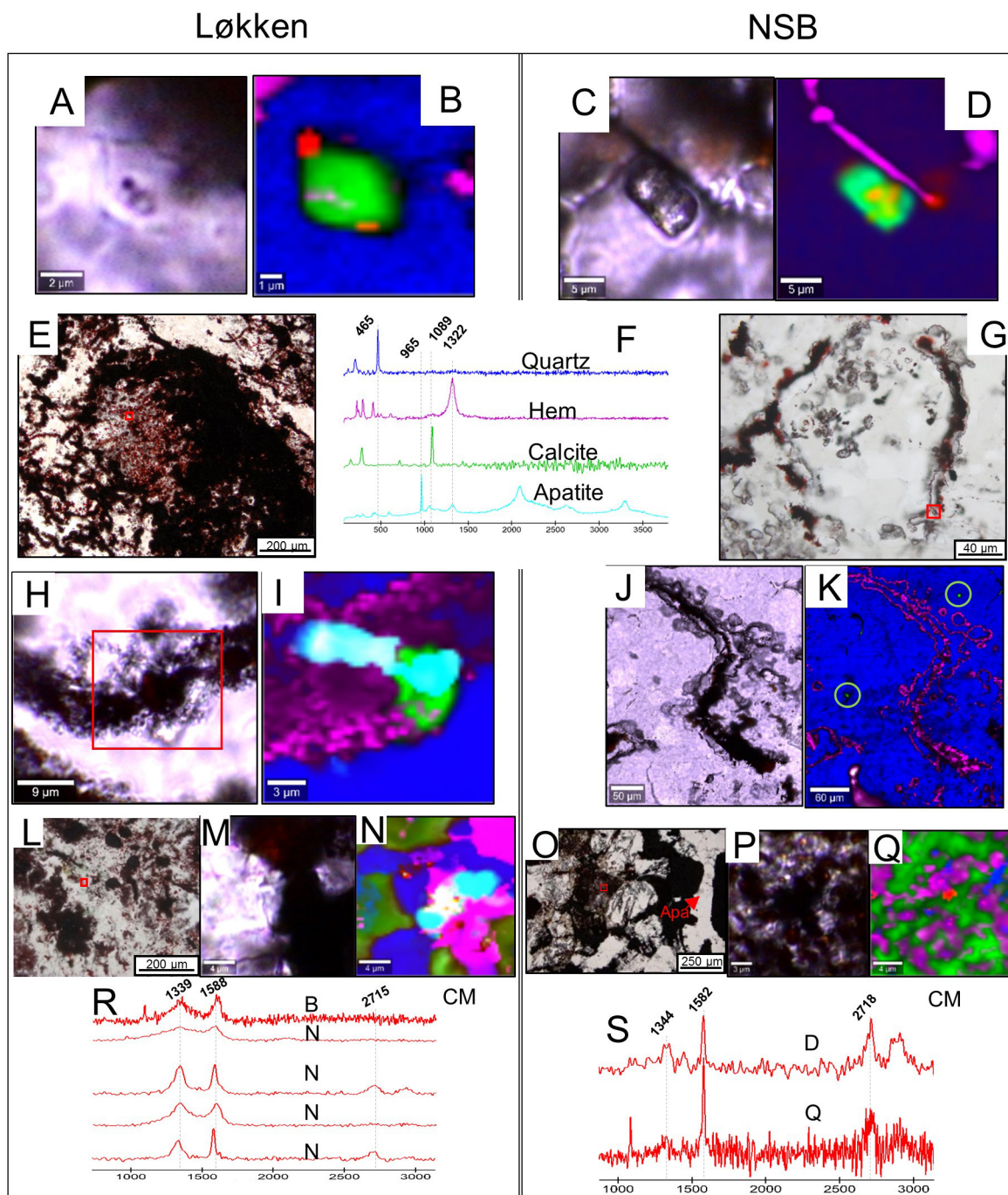
Extended Data Figure 3 | Thin sections of samples in this study (see Supplementary Information for localities). Inset in **a** shows reflected light image of small, sub-spherical chalcopyrites with haematite. Red outlines mark haematite tubes and tube-like structures. Red arrows show the orientation of tubes. Blue circles highlight concretion structure in thin section and slab. Numbering of targets corresponds to Figures. Inset in **e** shows transmitted light image of carbonaceous material inside apatite lath. All sections are 2.5 cm wide, except rock slab (**f**) measuring 7 × 2 cm; Løkken-Høydal dimensions (**k–o**) are 2 × 6 cm, except JAH samples in **n**, which measure 2 × 8 cm.

Extended Data Figure 4 | Photomicrographs taken in plane-polarized light with reflected light of haematite tubes and filaments. Images in left column are taken at the surface of the thin section. Images in right column show a series of stacked images using the Z-project function in ImageJ. Stacked images are formed of 8–9 sequential images taken at 2-μm intervals through the thin section. **a**, Branching haematite filament. **b**, Stacked image of **a**. Arrows point to loose coils. **c**, **d**, Hollow tube truncated partially at the surface showing both the top (**c**, red arrow) and bottom surface (**d**, black arrow) of the tube. **e**, Twisted haematite filaments emanating from haematite kno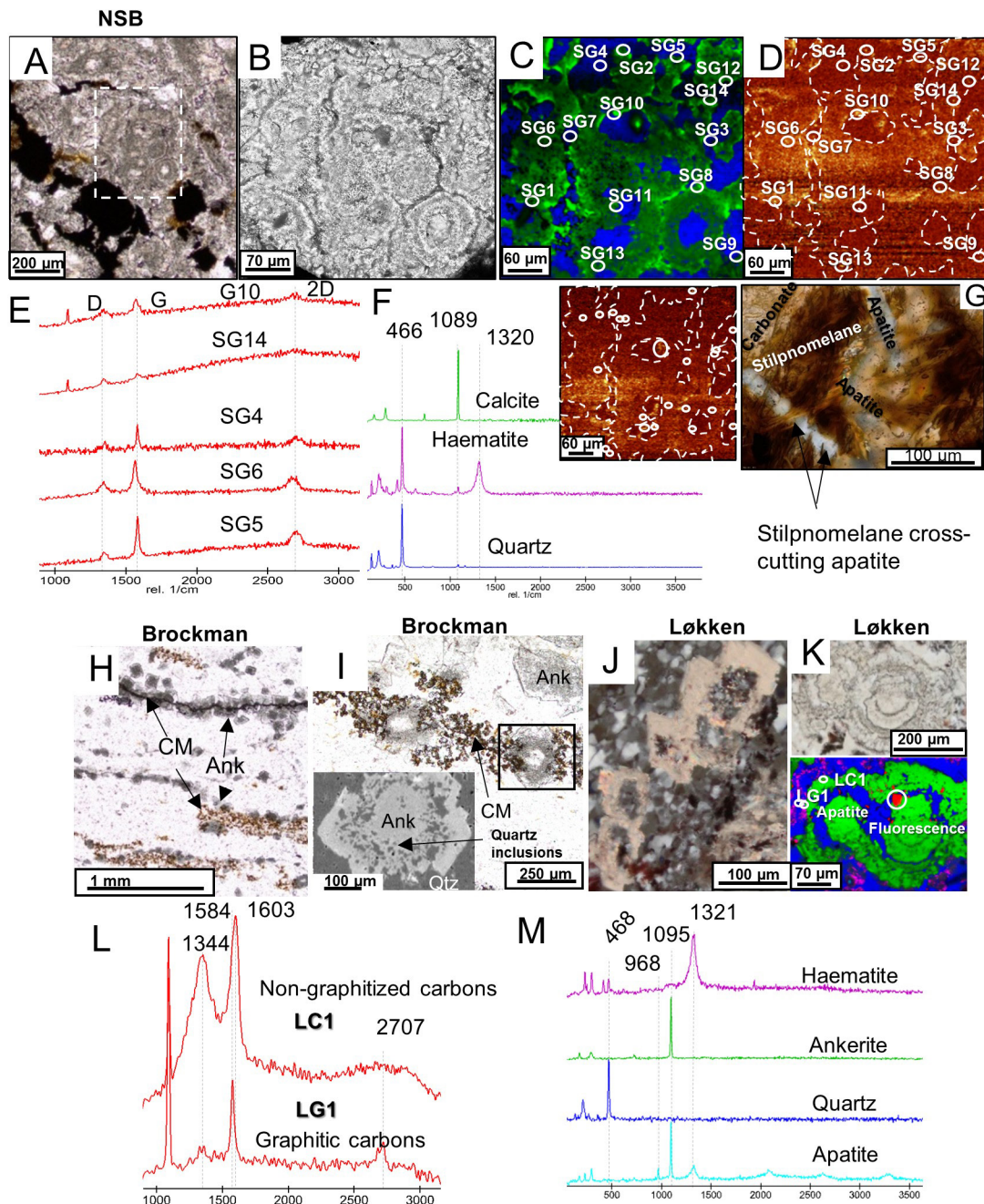b at varying angles and depths through the thin section. Inset shows aligned haematite crystals in filament indicative of twisting; arrow points to three tightly aligned plates. **f**, Stacked image of **e** with insets of candidate twisted stalks formed of aligned haematite plates; arrows show twist points. Dashed red boxes correspond to areas of insets. **g**, Filament diameter measurements from NSB (blue) and Løkken-Høydal (orange) jaspers. Filament diameters for NSB: $n = 23$, s.d. $= 2.8$ μm, avg $= 8.3$ μm; for Løkken-Høydal: $n = 28$, s.d. $= 1.9$ μm, avg $= 9.1$ μm. **h**, Tube diameters $n = 40$, s.d. $= 6.3$ μm, avg $= 24.9$ μm for NSB; $n = 40$, s.d. $= 3.1$ μm, avg $= 19.5$ μm for Løkken-Høydal.

Extended Data Figure 5 | Carbonate–apatite and carbonaceous material in the NSB and Løkken jaspers in association with haematite filaments.
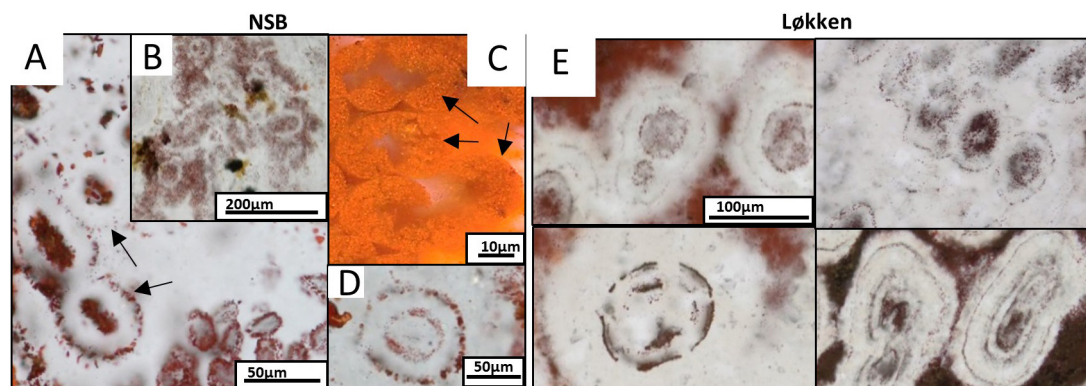a, b, Transmitted light and Raman images of carbonate associated with carbonaceous material inside a filament mat. c, d, Transmitted light and Raman images of carbonate associated with graphite in the NSB jasper associated with a filament. e, Contextual image of the carbonate grain (red box) with haematite filaments. f, Raman spectra of minerals mapped in this figure. g, Contextual image of carbonate grain (red box) with haematite filaments. h, i, Transmitted light and Raman images of haematite filament in Løkken jasper, associated with apatite and carbonate grains. j, k, Transmitted light and Raman images of haematite filament in NSB jasper associated with carbonate grains (green circles). l, Contextual image of apatite associated with carbonaceous material and carbonate within millimetres of filaments in the Løkken jasper. m, n, Transmitted light and Raman images of apatite grain. o, Contextual image of graphite in carbonate spatially occurring within millimetres of haematite filaments and apatite in the NSB. p, q, Transmitted light and Raman images of graphite particle in carbonate. r, Raman spectra of carbonaceous material in Løkken jaspers from b and n. s, Raman spectra of carbonaceous material in NSB jaspers from d and q.
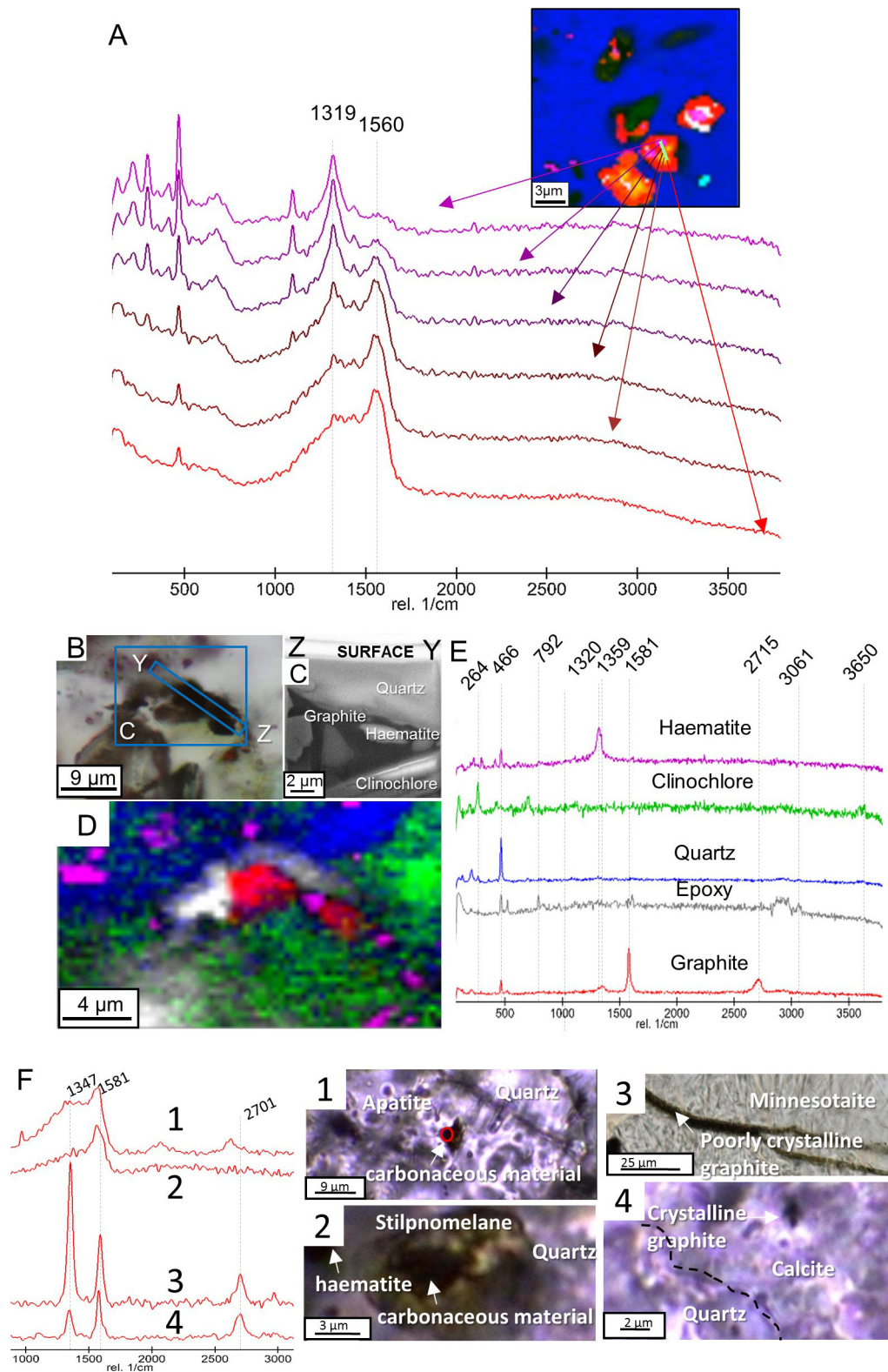
Extended Data Figure 6 | Carbonate rosettes. a, Transmitted light image of calcite rosettes from the NSB. **b, c,** Transmitted light and Raman images of target area (dashed outline from **a**). **d,** Graphite Raman filter map (filter: 1,580 cm^{-1}, width 40 cm^{-1}). Circled pixels are graphite grains. **e,** Raman spectra of selected graphite particles. **f,** Average Raman spectra for Raman map in **c** with inset of haematite Raman filter map (filter: 1,320 cm^{-1}, width 30 cm^{-1}). Circled pixels are haematite grains. **g,** Stilpnomelane laths overgrowing apatite in the NSB. **h,** Ankerite rhombohedra envelop a layer of carbonaceous material in the Dales Gorge Member of the Brockman iron formation. **i,** Ankerite rosettes with quartz inclusions in a carbonaceous material layer. **j,** Ankerite rosette with quartz core from the Løkken jasper. **k,** Ankerite rosettes overgrowing haematite filaments (top) and corresponding Raman map (bottom). **l,** Selected carbon spectra showing diversity of carbon preservation. Non-graphitized carbon is the most abundant variety in the rosettes. **m,** Average Raman spectra from map.
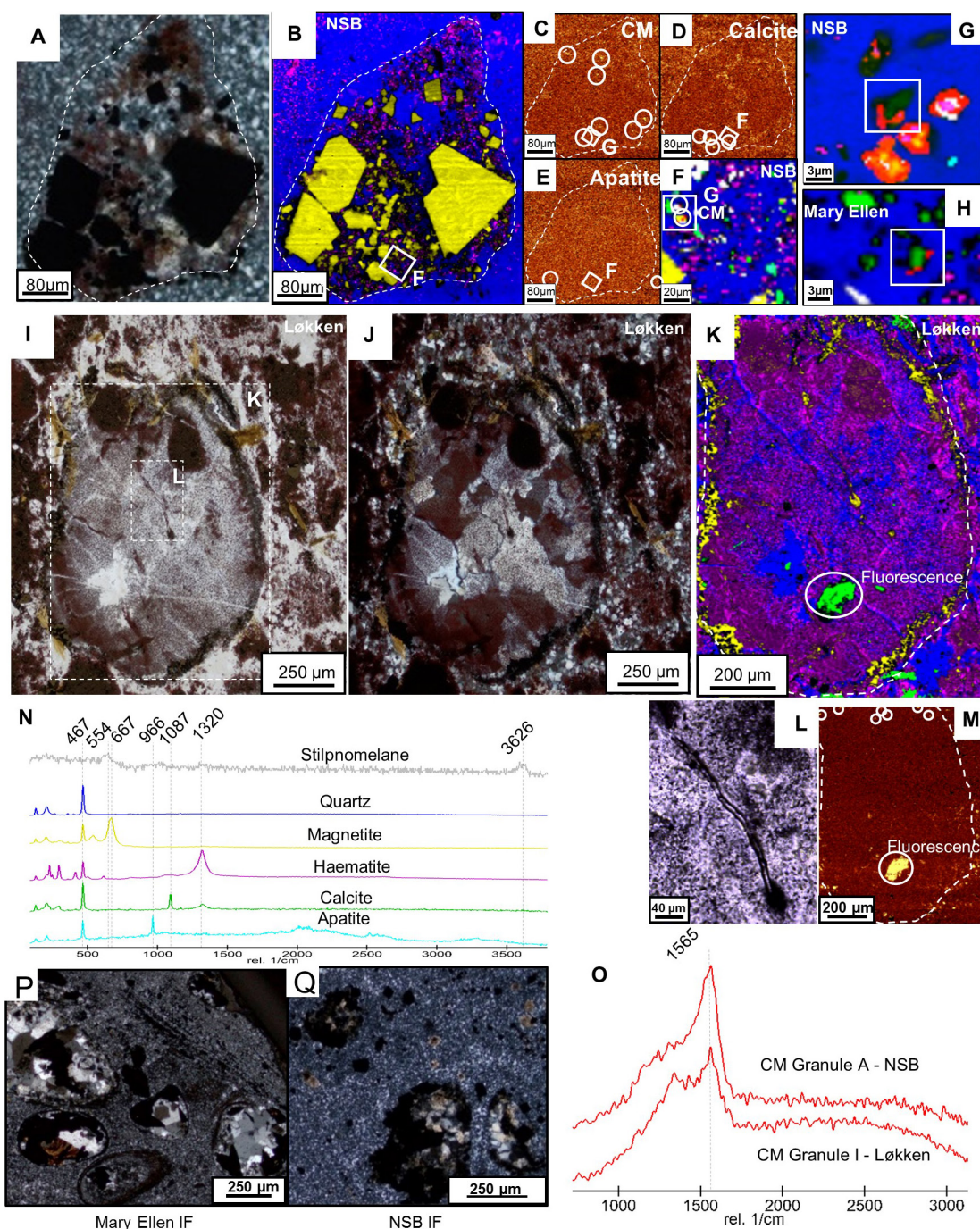
Extended Data Figure 7 | Transmitted light and reflected light images of haematite rosettes. a–d, From NSB; **e**, from Løkken jaspers. **a**, Large (60 μm) haematite rosettes (arrows) with cores. **b**, Haematite rosettes in dense haematite. **c**, Deformed, thicker-walled (25 μm) haematite rosettes (arrows). **d**, Concentric haematite rosette. **e**, Haematite rosettes from Løkken jaspers, same scale bar for all.

Extended Data Figure 8 | Variety of graphic carbons from the NSB.
a, Carbonaceous material Raman spectra, showing the transition between haematite and carbonaceous material. The 1,320 cm^{-1} haematite peak produces a disordered carbonaceous material spectrum. However, the G-peak position shows that such carbonaceous material is not disordered carbonaceous material like immature kerogen, which peaks around 1,610 cm^{-1}. The Raman spectra are taken from a section (green line) across a carbon particle in the Raman map inset, which has a 330-nm spatial resolution. Note the inclusions of haematite (pink) in the carbonaceous material (red). All other colours and mineral spectra for the Raman map are in Extended Data Fig. 9g. **b**, Transmitted light image of graphic carbon particles from PC0822. **c**, Secondary electron image, looking down a focused ion beam trench through graphic carbon particles. **d**, Raman spectral map of boxed area from **b**. **e**, Raman spectra for phases in spectral map. **f**, 1. Disordered graphic carbon in apatite lath, transmitted light. 2. Disordered graphic carbon in a granule, transmitted light. 3. Poorly crystalline graphic carbon vein, transmitted light. 4. Crystalline graphic carbon in a carbonate rosette, transmitted light.

Extended Data Figure 9 | Granules from the NSB and from the Løkken jaspers. a, Transmitted light image of a granule in the NSB. **b**, Raman map of the granule in **a**. **c**, Carbonaceous material Raman filter map (filter: 1,580 cm^{-1}, width 80 cm^{-1}). **d**, Calcite Raman filter map (filter: 1,089 cm^{-1}, width 20 cm^{-1}). **e**, Apatite Raman filter map (filter: 965 cm^{-1}, width 30 cm^{-1}). **f**, One micrometre spatial resolution Raman scan of part of the granule in **a**. **g**, Raman scan (360 nm resolution) of boxed area in **f** (yellow and white colours are colour combination artefacts). **H**, Raman scan (500 nm resolution) of a portion of the interior of the Mary Ellen granule in Fig. 4b, showing carbonaceous material coating a carbonate grain, like carbonaceous material coating a carbonate grain in the NSB granule in **a**. **i**, Transmitted light image of granule from the Løkken jasper.

j, Granule in **i**, viewed in cross-polarized light. Note the characteristic internal quartz recrystallization, relative to the matrix. **k**, Raman map of the granule in **i**. Note that magnetite forms a rim around the granule as in the NSB and Biwabik granules (Fig. 4). **l**, Microfossil within a granule preserved in haematite. The morphology shows the characteristic terminal knob of iron like the larger tubes preserved in the NSB. **m**, Carbonaceous material Raman filter map (filter: 1,566 cm^{-1}, width 60 cm^{-1}). **n**, Average Raman spectra for all Raman maps in this figure. **o**, Representative carbonaceous material spectra from granules in this figure. **p, q**, Cross-polarized images of iron-bearing granules from the Mary Ellen, Biwabik (**p**) and NSB (**q**) iron formations showing relative quartz recrystallization and magnetite rims.